The Mechanical Properties of 3D Woven Composites

Umer, R.[1*], Alhussein, H.[1], Zhou, J.[2], Cantwell, WJ.[1]

[1] Aerospace Research and Innovation Center (ARIC), Khalifa University of Science, Technology and Research (KUSTAR), Po.Box127788, Abu Dhabi, UAE.
[2] School of Engineering, University of Liverpool, Liverpool, L69 3GH, U.K.
*Corresponding Author Email: rehan.umer@kustar.ac.ae
Ph: +971-2-5018337

Abstract:

In this work, three types of 3D woven fabric (orthogonal, angle interlock and layer-to-layer) were used to study the effect of weaving architecture on processing and mechanical properties. In order to characterize the fabrics for liquid composite molding (LCM) processes, the compaction and permeability characteristics of the reinforcements were measured as function of fiber volume fraction. High compaction pressures were required to achieve a target fiber volume fraction of 0.65, due to presence of through-thickness binder yarns that restricts fiber nesting. In-plane permeability experiments were completed and flow front patterns were obtained to understand the anisotropy in the laminates. The RTM process was then used to manufacture panels that were then tested under quasi-static flexure and low velocity impact conditions. It was found that the flexural strength and modulus was higher along the weft direction, where high in-plane permeability of the reinforcement was observed, due to fiber alignment. Impact tests on composite plates based on the three types of fabric indicated that the orthogonal system offered a slightly higher perforation resistance and lower levels of damage at any given energy.

Keywords: Liquid Composite Molding, 3D fabrics, Mechanical properties

1.0 Introduction

The term Liquid Composite Molding (LCM) describes a number of processes, in which dry fibrous reinforcements are draped on a mold to create a preform, the mold is then closed and the preform is impregnated with a polymeric resin to displace the trapped air. Glass and carbon textiles are normally used as reinforcements. The quality and mechanical properties of a composite part is mainly characterized by two parameters; these being the fiber volume fraction (V_f) and the defects present, mostly as void content. In general, higher V_f means superior mechanical properties and stronger parts. When the dry preform is enclosed between rigid molds, the V_f can be accurately controlled by the cavity thickness. Hence, a higher and more uniform V_f is achieved using the LCM process than traditional hand lay-up techniques. LCM processes are mainly categorized into three major variants; e.g. resin transfer molding (RTM), compression RTM (CRTM) and vacuum assisted RTM (VARTM). The process selection depends on two parameters; the end-product requirements (mechanical properties, quality and surface finish) and the process requirements (size, cycle time, and labor costs). In RTM, the reinforcement, traditionally a two dimensional (2D) fabric, is placed in the lower mold cavity. The upper rigid mold closes the cavity containing the preform and holds it under a clamping force. Clamping forces are usually applied through a press or mechanical clamps. The V_f is controlled by the cavity thickness. The resin is injected in the mold from one or multiple gates.

The preform offers resistance to flow, known as permeability of the fiber bed. High V_f may cause very slow flow fronts at low pressures and high viscosity. Hence, an optimization of the process parameters is required [1, 2]. RTM molds are typically made of steel or aluminum and can be both heavy and expensive. When manufacturing large parts, larger presses are required and high

injection pressures become essential, which can significantly increase the cost of the process. These factors render the RTM process more suited for small parts with very tight geometrical tolerances. The whole process can be automated in operations such as, preforming, resin injection and de-molding. During mold closure in LCM, changes in the internal structure of the fabric play an important role in determining the mechanical properties and failure mechanisms of the finished composite part.

2D fabrics have been extensively used in the manufacture of composite structures over the past 50 years or so. More recently, advanced textile weaving techniques have been used to produce 3D textiles for composite processing. A detailed description of the 3D weaving process has been given by a number of researchers [3-6]. Three dimensional woven reinforcements are prepared in alternating non-crimped layers of weft and warp yarns. The binder yarns hold these layers together, increasing the interlaminar strength of the resulting composite. The most common production techniques for 3D textiles are weaving, braiding and knitting [4]. The mechanical properties can be tailored by having different binder yarn paths. In 3D textiles, it is possible to weave near net-shape and complex structures. Stiffeners and stringers are common examples of single piece 3D preforms. Three dimensional fabrics can help overcome many delamination problems. Zikry *et al.* [7-9] showed that 3D woven composites have a better damage resistance than 2D woven composites, due to the interactions of surface wefts and z-crimps. 3D woven composites can dissipate energy over a large area with superior perforation strength than 2D woven composites [7]. Rao *et al* [10] showed with experimental contour mapping of several failure modes that the z-yarns effectively isolate the interlaminar cracks.

The incentive for using 3D textiles in composites has been motivated by several needs; e.g. to reduce processing costs by reducing laying-up times, increase the through-thickness strength of the component whilst reducing the likelihood of delamination. Although there has been significant work on the properties and failure of 3D woven composites under quasi-static and impact loading [11-19], there are few published studies on the compaction characterization of 3D fabrics as reinforcements for LCM processes [20-24]. Endruweit *et al.* [23] concluded that different fabric architectures exhibited different compression mechanisms during LCM processing. For an angle interlock weave at high compression levels, the main mechanism is the change in bundle cross section. In contrast, the main controlling mechanism in an orthogonal fabric is the compaction behavior of the through thickness z-fiber bundles. Polturi and Sagar [24] studied the compression response of different 3D weaving patterns and validated a model based on an energy-minimization technique using their experimental data. The impregnation of liquid resin in thick 3D preforms is expected to be more complex than 2D preforms. More specifically, the z-binder fibers effectively influence both the in-plane and through-thickness permeability [25-31]. To date, a thorough investigation of LCM processing and its effects on mechanical performance of 3D woven composites is lacking.

Here, we investigate the potential of using 3D woven reinforcements in LCM processes and characterize the mechanical properties of the resulting composite plates. Initially, the compaction and permeability responses of 3D reinforcements are studied. One of the key challenges faced when using 3D reinforcements is to overcome the through-thickness stiffness, due to the z-binder yarns. The binder yarns tend to restrict movement of adjacent tows and prevent nesting, resulting in an increased resistance to deformation in the through-thickness direction. As a result, the

reinforcement generally achieves a low V_f under vacuum pressure, if VARTM process is used. Due to high tooling forces required to achieve V_f values greater than 60%, RTM process was selected as best manufacturing route for the selected reinforcements. Experimental mold filling times were obtained and compared with analytical solutions using a simple 1D rectilinear filling. Flexural and impact tests were carried out on three different 3D fabrics. The damage in the manufactured plates was analyzed using optical microscopy and x-ray micro computed tomography (XCT).

2.0 Experimental Procedure

2.1 Materials

Three different types of 3D reinforcement, supplied by Sigmatex, UK, were investigated in this study. It was expected that these three reinforcement architectures would exhibit different behaviours in terms of processing and mechanical properties. The z-binder yarns in all three architectures have different paths or orientations to hold the weft and warp fibers together, see Figure 1. Fabrics in Figure 1a and 1b are orthogonal and angle interlock respectively, each fabric having eight layers of 12K carbon fiber warp, nine layers of weft and 6K through-thickness z-yarns acting as binder yarns. Fabric in Figure 1c is a layer to layer fabric with six weft layers and five warp layers with interlacing yarns. In an angle interlock weaving process, the z-binder tows are woven at an angle, which is called the undulation angle, with the warp direction. Whereas in an orthogonal interlock weaving procedure, the z-binder tows are placed through the thickness direction of the fabric that interlaces together all the layers. In layer to layer interlocking process, a binder tow interlaces one, or a few adjacent layers. The orthogonal fabrics can provide better

fiber volume fraction in a composite compared to angle interlock fabrics, while the angle interlock fabrics may have better distortion capability and flexibility than the orthogonal fabrics. The layer to layer interlocking can also offer better fiber volume fraction due to the overlapping arrangement of binders in the thickness direction [3]. It is anticipated that orthogonal fabrics will produce composites with better through thickness performance, whereas layer to layer and angle interlock fabrics will produce complex configurations.

2.2 Reinforcement Characterization

Compaction Response

Dry compaction tests were carried out in a 150 mm x 150 mm square steel fixture installed in an MTS universal testing machine. A 300 kN load cell was attached to the moving crosshead of the machine. A compressive load was applied to 100 mm x 100 mm sample up to a target fiber volume fraction of 0.65, then holding the displacement and allowing the stress to relax for 10 minutes. In an actual LCM process, the dry compaction represents mold closing and the hold period when the resin is being injected. The compaction tests were conducted to determine the tooling forces required to compress to $V_f = 0.65$. All tests were performed at a constant crosshead displacement rate of 0.033 mm/s.

Permeability Measurements

In this study, permeability measurements were conducted on a purpose-built radial, in-plane permeability rig [31]. Similar radial permeability test rigs were used in previous studies [32-34]. The test fixture consists of a 300 mm square toughened glass plate mounted in an aluminum

frame. The rig was installed on an MTS testing machine with a maximum load capacity of 300 kN. The reinforcements were compressed from above using a 250 mm diameter circular steel plate. The steel plate contained a 10 mm diameter hole in its center through which fluid was injected. The injection pressure was measured using a pressure transducer mounted on the top plate. The test fluid used in this study was Shell Tellus S2 M32, a hydraulic oil with a room temperature (23^{o}C) viscosity of 0.052 Pa.s. The use of such a fluid, rather than a resin, avoids unwanted effects associated with curing of the resin during the test. The hydraulic oil was injected using a pressure pot, that was in turn connected to a compressed air supply. The location of the flow front during the test was continuously monitored using a high definition 8MP camera positioned directly under the glass plate. The flow front was illuminated using a simple light source. A computer with data acquisition software (LabVIEW) was used to record the injection pressure. In order to ensure in-plane radial flow in the preforms, a 10 mm hole was created using a metal punch. The preform was positioned on the glass plate and aligned to ensure that the hole was aligned with the opening in the upper platen.

At the start of the test, a compressive pre-stress was applied to the preform and this was followed by loading at 0.033 mm/s to the ultimate required fiber volume fraction (values of 0.45, 0.50, 0.55 and 0.65 were considered here). The crosshead displacement was then maintained constant for approximately two minutes to monitor the resulting stress relaxation. The hydraulic oil was then injected at a constant pressure of 150 kPa. Information from the pressure transducer, the universal test machine and the camera was recorded. Finally, the flow front data was post processed using the image processing capabilities in Matlab software package.

2.3 RTM Experiments

A 400 mm x 400 mm square aluminum mold was designed for the RTM experiments. The mold cavity size was 250 mm x 250 mm x 2.8 mm. To achieve different values of V_f, the bottom half can be replaced with another half with a different thickness. Depending on the injection strategy, the upper mold half has several ports to be used as gates and vents. The ports that were not in use were closed using a plug. This configuration enables the mold to be used in both rectilinear and radial injection strategies (see Figure 2). In order to achieve target V_f of approximately 0.65, the mold was placed in a 100 ton heated hydraulic press (Carver Press, USA) (Figure 2b). A two part epoxy resin system, Gurit Prime 20 LV™ with a slow hardener was injected using the *iject* RTM injection system supplied by *Wolfangel, Germany* (Figure 2c). This system has an automatic dosing unit for resin mixing. The flow rate was measured by the number of strokes the system makes during the injection. The maximum allowable pressure can be set in the machine. The inlet pressure was recorded using a pressure transducer connected to the inlet.

The 3D reinforcement samples were cut to the mold cavity dimensions. A mold release wax was applied to the two halves of the mold for easy removal of the part. The reinforcements were placed in the mold cavity, and the mold was placed in the press using a sliding table. A rectilinear injection strategy was adopted in the weft direction. In this direction, the permeability was higher, thereby reducing the filling time during the experiment. To prevent race tracking (edge effects), a silicon seal was applied along the edges. A constant injection pressure was applied by the machine. After checking the mixing ratio, the injection valve was opened and the flow continued until the resin appeared from the vents. After that, the injection gates and vents

were clamped. Based on the manufacturer's cure cycle, the mold was heated to 65^{o}C and the resin was left to cure for 7 hours.

The total mold filling time t_{fill} was compared with experiments and values obtained from analytical solutions [35] of a unidirectional flow in a flat geometry were derived from Darcy's law;

$$t_{fill}=\frac{\mu(1-V_f)L^2}{K_{xx}P_{inj}\ 2} \qquad (1)$$

Where μ is resin viscosity (0.3 Pa.s), K_{xx} is the permeability in the flow direction, P_{inj} is the injection pressure and L is the total flow length (0.25 m), other parameters are given in Table 1.

2.4 Flexural Testing

Five specimens for each 3D fabric with dimensions of 120 mm x 13 mm x 2.8 mm were cut along weft and warp directions in preparation for flexural testing. Flexural tests were conducted using a three-point bending rig, with the hemispherical supports positioned to maintain a span to thickness ratio of 32:1. The rig was mounted on an Instron 4505 universal testing machine and the crosshead displacement rate was maintained at 1 mm/min. All tests were performed according to ASTM D7264. Micro CT scans were undertaken after flexural testing using the GE Phoenics nanotom® XCT scanner.

2.5 Impact Testing

Impact tests were conducted on the three types of CFRP panel, using the falling-weight impact facility shown schematically in Figure 3. Here, test square specimens, with dimensions of 130 x

130 mm, were supported by a steel ring with a 100 mm internal opening and impacted by a falling carriage with a 12.5 mm steel hemispherical head. The impact energy was varied between 5 Joules and 40 Joules by increasing the carriage mass up to 2836 grams. For the majority of tests, the release height of the falling carriage was approximately 1.6 meters. Table 2 summarizes the impact energies, the associated carriage masses, release heights and impact velocities. After impact, the carriage was caught manually in order to avoid unwanted secondary impacts. The impact load was recorded using a piezoelectric load-cell located immediately above the hemispherical indentor and the associated displacement of the target was monitored using a high speed video camera positioned in front of the impact rig. The absorbed energies were then calculated by integrating the merged area under the load-displacement traces. After testing, both the front and rear surfaces of the specimens were photographed to elucidate any prevailing damage. Finally, a number of samples were sectioned, polished in order to investigate the failure mechanisms occurring during impact loading.

Following impact testing the flexural strength of the panels was assessed by conducting quasi-static tests on the circular plates supported under the same conditions as those used during impact tests. This testing mode was selected since it was considered to be a more appropriate mode of testing and avoided the need to remove beam-like specimens, that would be heavily damaged and unrepresentative of the larger structure, from the centers of the panels. Here, plates were supported on a steel ring with an internal diameter of 100 mm and loaded by a 20 mm diameter steel indentor. It should be noted that this indentor was larger than that used during impact tests to avoid it simply pushing through the perforation zone in the heavily-damaged plates.

3.0 Results and Discussion

3.1 Compaction Response

Dry compaction experiments were conducted to determine peak forces required to compress the reinforcements contained inside a mold to the target thickness or fiber volume fraction. Figure 4 shows dry compaction curves (stress versus time) after achieving a target thickness corresponding to 0.65 V_f, for each type of reinforcement. After reaching the peak value, the stress drops instantaneously and continues to relax until there is no further evident drop. The orthogonal fabrics compacted at around 2.3 MPa peak stress, whereas the layer to layer fabrics offered the lowest peak stress values of approximately 1 MPa. The angle interlock fabrics exhibited a stress level of approximately 2.0 MPa. Due to reduced nesting effects between the tows, the meso-scopic spaces remained opened in the fabric during compaction, before mold filling. Usually, in a 2D fabric, the compaction of a fiber reinforcement begins with a gap reduction between the weft and warp tows, once the inter-tow gap reduces, the tows start to flatten and nest with adjacent tows. The orthogonal fabrics were found to be stiff, due to the tightly woven patterns of the vertical z-binder yarns. In the orthogonal and angle interlock fabrics, the tows did not expand freely, due to the presence of the vertical z-binder yarns, hence higher compaction loads were required. As a result, in an actual LCM process such as RTM, the orthogonal and angle interlock fabrics will require high tooling forces or will compact to a lower fiber volume content under 1 atm (100 kPa) vacuum pressure, such as with VARTM.

3.2 Permeability Measurements

Figure 5 presents the in-plane permeability results for all of the 3D fabrics tested, showing the influence of reinforcement architecture on the permeability. These tests were conducted to determine the principal permeability values for a range of fiber volume fractions. Figure 6 shows photographs of flow front profiles of each type of reinforcement at three different V_{fs}. The components of the in-plane permeability tensor are defined as the principal directions of the ellipse observed at the flow front. Often, these principal directions are different from the warp and weft directions, but in our case the angle of deviation from principal direction was negligible. For all of the reinforcements tested here, Figure 5 shows that the permeability in the warp (K_{22}) direction was consistently lower than the weft (K_{11}) direction. The orthogonal and angle interlock preforms exhibited the highest values of permeability at low V_f. This was due to the presence of large meso-scopic gaps around the z-binder yarns, which can be clearly seen in the XCT scans in Figure 1. The layer to layer fabric exhibited more elliptical flow front profiles with greater differences between the two principal permeability values. In the orthogonal preforms, at 0.65 V_f, the binder yarns were flattened considerably, resulting in a reduction in the number of surface pores, causing the permeability values to converge towards the angle interlock permeability values. For the layer to layer preforms, the meso-scale gaps that run through the thickness were very few, giving the lowest rates of in-plane flow and the lowest permeability of the three fabrics considered.

3.3 RTM Experiments

The experimental values of permeability, injection pressures and V_f used in the RTM experiments at a cavity thickness of 2.8 mm are listed in Table 1. The permeability values were determined using the exponential fit to the permeability data. The RTM equipment uses constant

injection pressures for mold fillings hence, injection pressures of 1.5 to 2.4 bars were recorded at the injection gate using a pressure transducer. Since we used closed mold RTM, comparisons of flow front positions at different time intervals were not possible. Here, we only compare total mold filling times with analytical solutions, as shown in Table 1. The mold filling times were in good agreement with the predicted ones for all fabrics. A good co-relation between measured permeability and RTM results can be drawn here. According to permeability results, orthogonal and angle interlock preforms exhibited highest permeability in K_{11} direction, due to the presence of large meso-scopic gaps around the z-binder yarns, as shown in Figure 1. The layer to layer preforms showed lowest in-plane permeability values, as a result, the flow front progression was slowest, resulting in highest mold filling time.

3.4 Flexural Response

Figure 7 shows the flexural strength and modulus values for the three types of 3D fabric composite. The trends agree with the observations in Figure 6. The flow front patterns showed that fiber alignment in the weft (K_{11}) direction was very dominant in the layer to layer fabrics, hence a more pronounced elliptical flow front was recorded, leading to high flexural strength and modulus values compared to the warp (K_{22}) direction. If we compare all three fabrics, the differences in strength and modulus of the orthogonal and angle interlock fabrics was not significant, whereas, the differences in strength and modulus properties in warp and weft directions of the layer to layer fabric was very large. Figure 8 shows XCT images following flexural testing. Crack propagation initiated from resin-rich areas around z-binder yarns and propagated along the z-yarns with warp layer delamination in both the orthogonal and angle

interlock fabric composites. The cracks typically followed the binder yarn patterns. The layer to layer fabric exhibits a delamination-type failure (similar to that commonly observed in 2D fabrics) where the top most layers delaminated from remainder of the structure.

3.5 Impact Behavior of the Plates

Figure 9 shows impact load-displacement traces for the orthogonal and angle interlock systems The layer-to-layer traces were similar to the angle interlock and are therefore not included here. All of the curves exhibit an oscillatory response during the elastic phase of loading, due to ringing effects in the load-cell, induced by the initial contact between the indentor and the panel. These effects are also observed in fully clamped panels. They can be removed by filtering the impact traces at a frequency associated with this oscillatory response, however, this can result in the loss of information and was therefore avoided in the present case.

As expected, the maximum impact force increases with impact energy. For all energies up to 40 Joules, impact on the orthogonal composites did not result in perforation of the panel and the projectile therefore rebounded following contact. In contrast, the angle interlock panel exhibited significant damage following a 30 Joule impact and was perforated during a 40 Joule impact, resulting in the impactor becoming wedged in the panel following testing. Additionally, it is worth noting that the highest impact forces were recorded following tests on the orthogonal panels, with values up to 10 kN being observed following a 40 Joule impact. The load-displacement traces for the layer-to-layer composites were similar to those of the angle interlock systems, with these panels also being perforated at the highest impact energy of 40 Joules.

The energy absorbed during the impact event was calculated by determining the area under the load-displacement traces. Figure 10 shows a plot of the absorbed energy as a function of impact energy. At the lowest impact energies, the energy-absorbing response of the three panels is similar with the plates absorbing approximately 50% of the incident energy during 10 and 15 Joule impacts. Differences in response appear following impacts at energies of 20 Joules and above, with the orthogonal laminates absorbing less energy than its two counterparts. This continues up to impacts at 40 Joules, where the angle interlock and layer-to-layer absorb virtually all of the incident energy (i.e. they are perforated and the orthogonal exhibits a capacity to absorb greater levels of energy).

Figure 11 shows photographs of the front and rear surfaces of panels following an impact energy of 40 Joules. Damage in the orthogonal laminate is clearly less severe than that observed in the two remaining systems. Here, local denting and isolated cracking on the uppermost surface and fiber fracture on the lower surface is observed in the orthogonal panel. In contrast, the angle interlock and layer-to-layer exhibit an entrance hole as well as significant splitting and fiber failure as the projectile exited the rear surface. This is clearly seen in the images taken parallel to the rear surface, shown in Figure 11.

A more detailed understanding of the failure mechanisms occurring during impact was achieved by sectioning panels subjected to an incident energy of 25 Joules, Figure 12. Damage in the orthogonal laminate is clearly very limited, taking the form of denting, a small delamination adjacent to the impact location on the top surface, lower surface fiber fracture within the volume under the impactor. In contrast, damage was much more severe in the angle interlock and layer-to-layer laminates, where significant levels of fiber fracture, delamination and volumetric damage are evident in the photomicrographs.

The residual load-carrying capacity of the panels was assessed through a series of flexural tests at quasi-static rates of strain. It should be recalled that these flexural tests were conducted on the square panels, simply-supported on a similar steel ring that was used for the impact tests. The samples were loaded by a larger hemisphere than used for dynamic testing in order to avoid the possibility of the indentor simply pushing through the perforation region in the more heavily-damaged panels. Testing indicated that the orthogonal panels offered a superior load-bearing capacity relative to the layer to layer and angle interlock systems. For example, following an impact energy of 30 Joules, the orthogonal laminate offered a flexural strength that was over 50% higher than its two remaining counterparts. At 40 Joules, these differences were reduced, with the orthogonal laminate being 25% stronger than the angle interlock and just 5% stronger than the layer-to layer composite. Much of this improved performance is, however, linked to the fact that the undamaged flexural strength of the orthogonal panel is 17% and 35% higher than that of the angle interlock and layer to layer composites, respectively. In order to account for these differences in undamaged strength, the residual flexural properties of the three fabrics were normalized by the respective undamaged values and these values are plotted against impact energy in Figure 13. Here, it is evident that, at low and intermediate energies, there is not a significant difference between the residual properties of the three fabrics. Some differences are apparent at higher energies, with the layer to layer and possibly the orthogonal laminates, offering superior properties.

4.0 Conclusions

The focus of this study was to manufacture and mechanically characterize three different types of 3D woven fabric with high fiber volume content. Compaction characterization tests were carried out to determine the peak stresses required to compact the fabrics to the target fiber volume fraction of 0.65. Low pressure LCM processes, such as VARTM, use vacuum pressure for compaction and are not suitable for achieving a high fiber volume content in these 3D woven reinforcement systems, due to the very high compaction pressures involved. Among the three types of reinforcement, it was concluded that the orthogonal fabrics required the highest stress of approximately 2.3 MPa, whereas the layer to layer fabric, which was closer to a 2D fabric, required the lowest peak stress of approximately 1 MPa to achieve 0.65 V_f. In-plane permeability tests showed greater promise for the orthogonal and angle interlock fabrics, due to presence of meso-scale surface pores around the vertical z-binder yarns. The flow front patterns in the layer to layer fabric were more anisotropic, due to greater levels of fiber alignment in the weft direction. RTM experiments showed good agreement with predicted mold filling times obtained from analytical solutions for all cases. Layer to layer fabric showed slowest mold filling due to low in-plane permeability. The RTM mold filling results give good confidence in the measured permeability.

Flexural test showed that samples cut along the weft direction offered higher strength values compared to samples cut along warp direction, this confirmed the findings of the flow front study, where the highest permeability was along weft direction. Finally, low velocity impact testing has shown that the orthogonal fabrics exhibited slightly lower levels of damage and a higher perforation resistance than the layer to layer and angle interlock fabrics.

5.0 Acknowledgements

This research was performed as part of the Aerospace Research & Innovation Center (ARIC) program which is jointly-funded by Mubadala Aerospace & Khalifa University. The authors would also like to acknowledge the technical support from Mr. Jimmy Thomas, Mr. Pradeep George and Mr. Bittu Scaria.

6.0 References

[1] Ruiz E, Achim V, Soukane S, Trochu F, Bréard J. Optimization of injection flow rate to minimize micro/macro-voids formation in resin transfer molded composites. Composites Science and Technology. 2006;66(3-4):475-86.

[2] Leclerc JS, Ruiz E. Porosity reduction using optimized flow velocity in Resin Transfer Molding. Composites Part A: Applied Science and Manufacturing. 2008;39(12):1859-68.

[3] Ansar M, Xinwei W, Chouwei Z. Modeling strategies of 3D woven composites: A review. Composite Structures. 2011;93(8):1947-63.

[4] X. Chen, Ed., Advances in 3D Textiles. Cambridge: Woodhead Publishing, 2015.

[5] Tong L, Mouritz AP, Bannister M. 3D Fibre Reinforced Polymer Composites: Elsevier; 2002.

[6] Hu J. 3-D fibrous assemblies: properties, applications and modeling of three-dimensional textile structures: Woodhead; 2008.

[7] Baucom JN, Zikry MA. Evolution of Failure Mechanisms in 2D and 3D Woven Composite Systems Under Quasi-static Perforation. Journal of Composite Materials. 2003;37(18):1651-74.

[8] Baucom JN, Zikry MA, Rajendran AM. Low-velocity impact damage accumulation in woven S2-glass composite systems. Composites Science and Technology. 2006;66:1229–38.

[9] Bahei-El-Din YA, Zikry MA. Impact-induced deformation fields in 2D and 3D woven composites. Composites Science and Technology. 2003;63:923–42.

[10] Rao PM, Walter TR, Sankar B, Subhash G, Yen CF. Analysis of failure modes in three-dimensional woven composites subjected to quasi-static indentation. Journal of Composite Materials. 2014;48(20):2473–91.

[11] Naik NK, Sekher YC, Meduri S. Damage in woven-fabric composites subjected to low-velocity impact. Composites Science and Technology. 2000;60:731-44.

[12] Asaee Z, Shadlou S, Taheri F. Low-velocity impact response of fiberglass/magnesium FMLs with a new 3D fiberglass fabric. Composite Structures. 2015;122:155-65.

[13] Karkkainen RL, Tzeng JT. Micromechanical Strength Modeling and Investigation of Stitch Density Effects on 3D Orthogonal Composites. Journal of Composite Materials. 2009;43(25):3125-42.

[14] Labanieh AR, Legrand X, Koncar V, Soulat D. Evaluation of the elastic behavior of multiaxis 3D-woven preforms by numerical approach. Journal of Composite Materials. 2014;48(26):3243–52.

[15] Jia X, Xia Z, Gu B. Micro/meso-scale damage analysis of three-dimensional orthogonal woven composites based on sub-repeating unit cells. Journal of Strain Analysis. 2012;47(5):313-28.

[16] Dai S, Cunningham PR, Marshall S, Silva C. Influence of fibre architecture on the tensile, compressive and flexural behaviour of 3D woven composites. Composites Part A: Applied Science and Manufacturing. 2015;69:195-207.

[17] Brandt J, Drechsler K, Arendts F-J. Mechanical performance of composites based on various three-dimensional woven-fibre preforms. Composites Science and Technology. 1996;56(3):381-6.

[18] Chou S, Chen H-C, Chen H-E. Effect of weave structure on mechanical fracture behavior of three-dimensional carbon fiber fabric reinforced epoxy resin composites. Composites Science and Technology. 1992;45(1):23-35.

[19] Jin L, Niu Z, Jin BC, Sun B, Gu B. Comparisons of static bending and fatigue damage between 3D angle-interlock and 3D orthogonal woven composites. Journal of Reinforced Plastics and Composites. 2012;31(4):935-45.

[20] Mahadik Y, Brown KAR, Hallett SR. Characterisation of 3D woven composite internal architecture and effect of compaction. Composites Part A: Applied Science and Manufacturing. 2010;41(7):872-80.

[21] Vernet N, Trochu F. Analysis and modeling of 3D Interlock fabric compaction behavior. Composites Part A: Applied Science and Manufacturing. 2016;80:182-93.

[22] Desplentere F, Lomov SV, Woerdeman DL, Verpoest I, Wevers M, Bogdanovich A. Micro-CT characterization of variability in 3D textile architecture. Composites Science and Technology. 2005;65(13):1920-30.

[23] Endruweit A, Long A. Analysis of compressibility and permeability of selected 3D woven reinforcements. Journal of Composite Materials. 2010;44(24):2833-2862.

[24] Potluri P, Sagar TV. Compaction modelling of textile preforms for composite structures. Composite Structures. 2008;68(1):177-185.

[25] Vernet N, Trochu F. In-plane and through-thickness permeability models for three-dimensional Interlock fabrics. Journal of Composite Materials. 2015;50(14):1951-69.

[26] Hoes K, Dinescu D, Sol H, Parnas RS, Lomov S. Study of nesting induced scatter of permeability values in layered reinforcement fabrics. Composites Part A: Applied Science and Manufacturing. 2004;35(12):1407-18.

[27] Liu HL, Hwang WR. Permeability prediction of fibrous porous media with complex 3D architectures. Composites Part A: Applied Science and Manufacturing. 2012;43(11):2030-8.

[28] Archer E, Buchanan S, McIlhagger AT, Quinn JP. The effect of 3D weaving and consolidation on carbon fiber tows, fabrics, and composites. Journal of Reinforced Plastics and Composites. 2010;29(20):3162-70.

[29] Song Y, Chung K, Kang T, Youn J. Prediction of permeability tensor for three dimensional circular braided preform by applying finite volume method to a unit cell. Composites Science and Technology, 2004;64(10):1629-1636.

[30] Mohamed M, Wetzel KK. 3D Woven Carbon/Glass Hybrid Spar Cap for Wind Turbine Rotor Blade. Journal of Sol. Energy Eng, 2006;128(4):562-573.

[31] Alhussein H, Umer R, Rao S, Swery E, Bickerton S, Cantwel WJ. Characterization of 3D woven reinforcements for liquid composite molding processes. Journal of Materials Science. 2016;51(6):3277-88.

[32] Meier R, Walbran A, Hahn C, Zaremba S, Drechsler. Methods to determine the permeability of textile reinforcements. Zeitschrift Kunststofftechnik/Journal of Plastics Technology. 2014;10(4):90-116.

[33] Liotier P-J, Govignon Q, Swery E, Drapier S, Bickerton S. Characterisation of woven flax fibres reinforcements: Effect of the shear on the in-plane permeability. Journal of Composite Materials. 2015;49(27):3415–3430.

[34] Swery E, Allen T, Comas-Cardona S, Govignon Q, Hickey C, Timms J, Tournier L, Walbran A, Kelly P, Bickerton S. Efficient experimental characterisation of the permeability of fibrous textiles. Journal of Composite Materils. 2016; In-press. DOI: 10.1177/0021998316630801.

[35] Lundström TS, Stenberg R, Bergström R, Partanen H, Birkeland PA. In-plane permeability measurements: a nordic round-robin study. Composites Part A: Applied Science and Manufacturing. 2000;31:29-43.

List of Tables

Table 1: RTM filling time comparisons

Fabric	Fiber Volume Fraction (V_f)	Injection Pressure (bars)	Permeability K_{11} (m^2)	Mold Filling Time (s)	
				Experiment	Analytical
Orthogonal	0.66	1.5	2.93E-11	769	725
Angle Interlock	0.63	2.4	2.27E-11	660	635
Layer to layer	0.65	2.0	1.14E-11	1560	1430

Table 2: Impact tests on CFRP with increasing energy

Test No.	Impact Energy (J)	Drop Height (m)	Impact Velocity (m/s)	Drop Weight (g)
1st	5	0.78	3.9	657.58
2nd	10	1.55	5.5	657.58
3rd	15	1.61	5.6	952.07
4th	20	1.43	5.2	1457.58
5th	25	1.54	5.5	1657.58
6th	30	1.58	5.6	1952.07
7th	35	1.78	5.9	2016.07
8th	40	1.47	5.3	2836.22

List of Figures

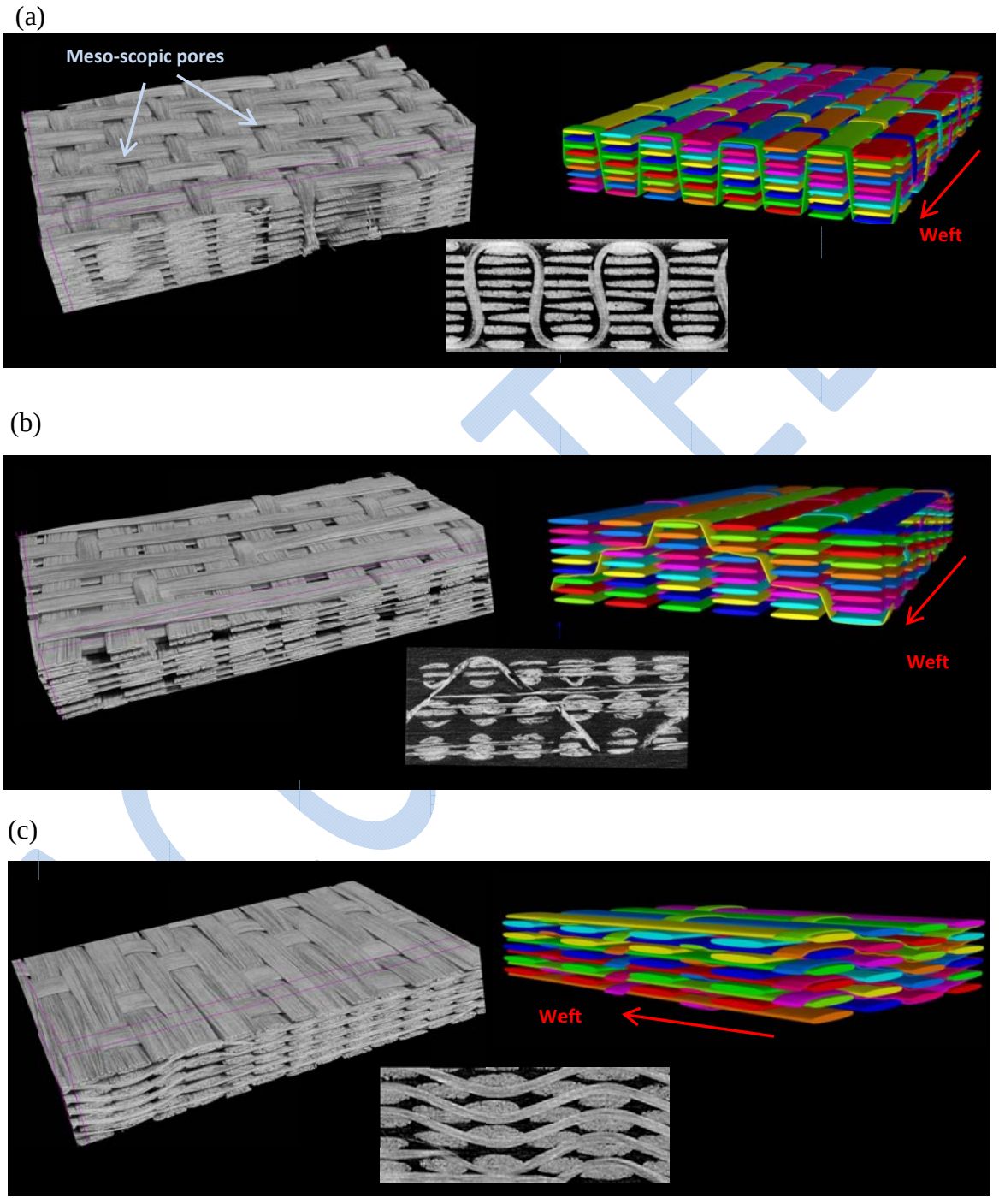

Figure 1. XCT scans and Texgen models of 3D fabrics (a) Orthogonal, (b) Angle interlock, (c) Layer to layer.

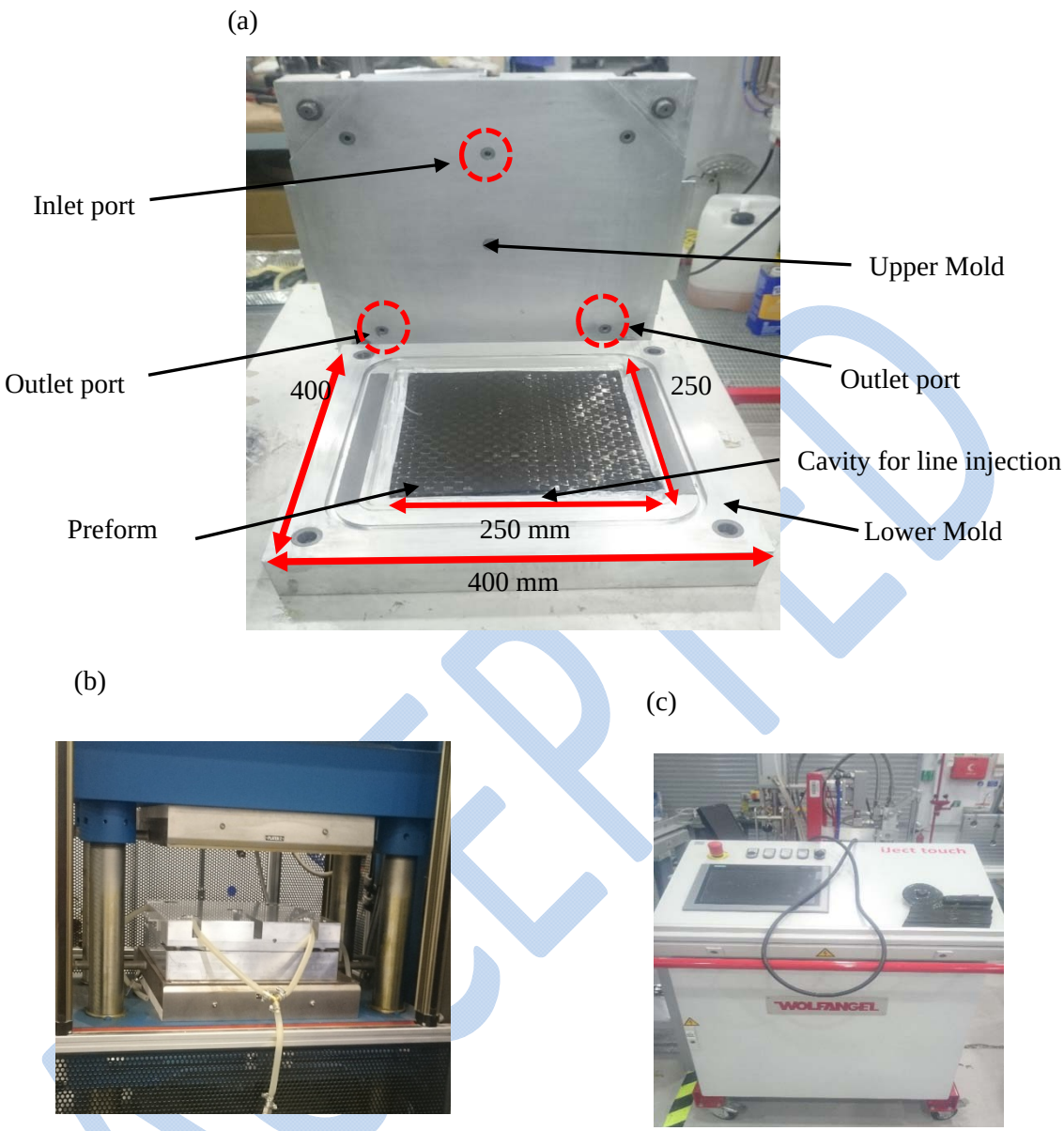

Figure 2. RTM set-up, (a) Upper and lower mold halves, (b) mold in 100 ton hot press (c) resin injection system.

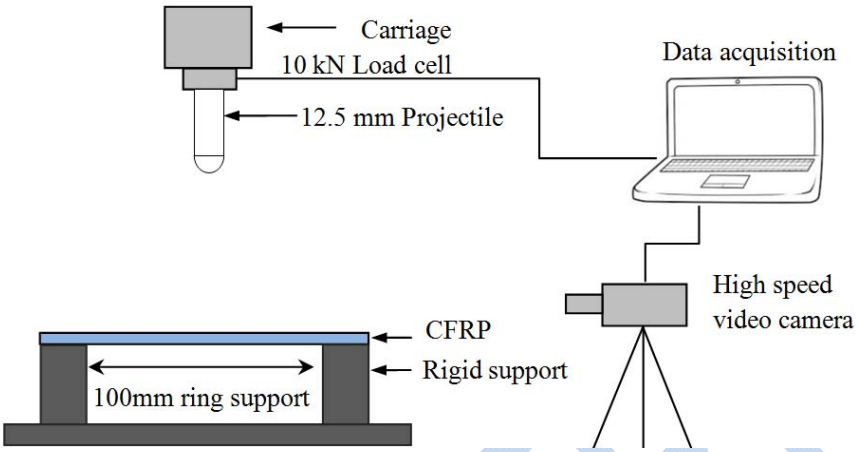

Figure 3. Schematic of drop-weight impact rig and clamped specimen.

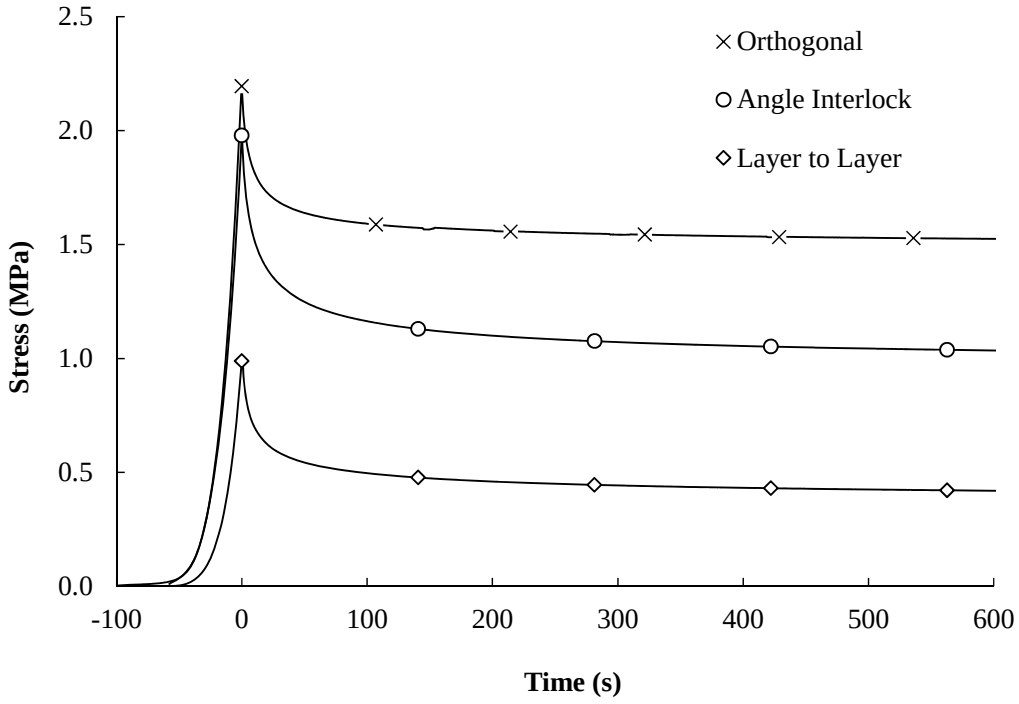

Figure 4. Dry compaction response of 3D fabrics.

(a)

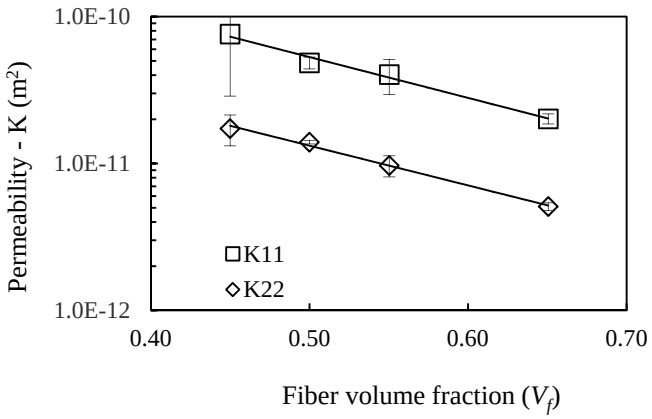

(b)

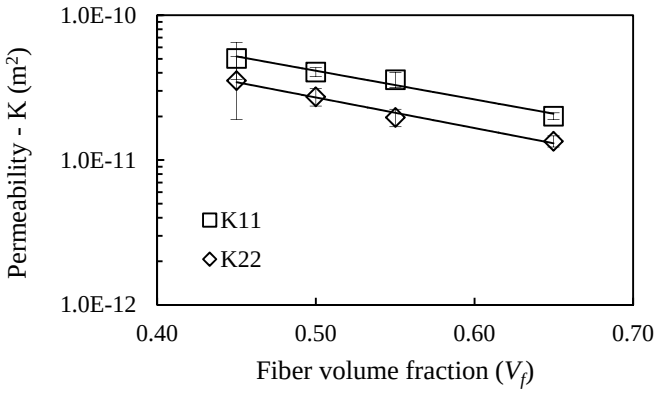

(c)

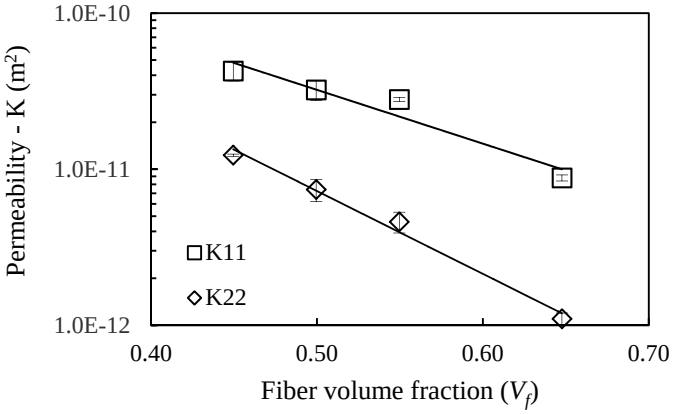

Figure 5. In-plane permeability of 3D fabrics (a) Orthogonal, (b) Angle interlock, (c) Layer to layer.

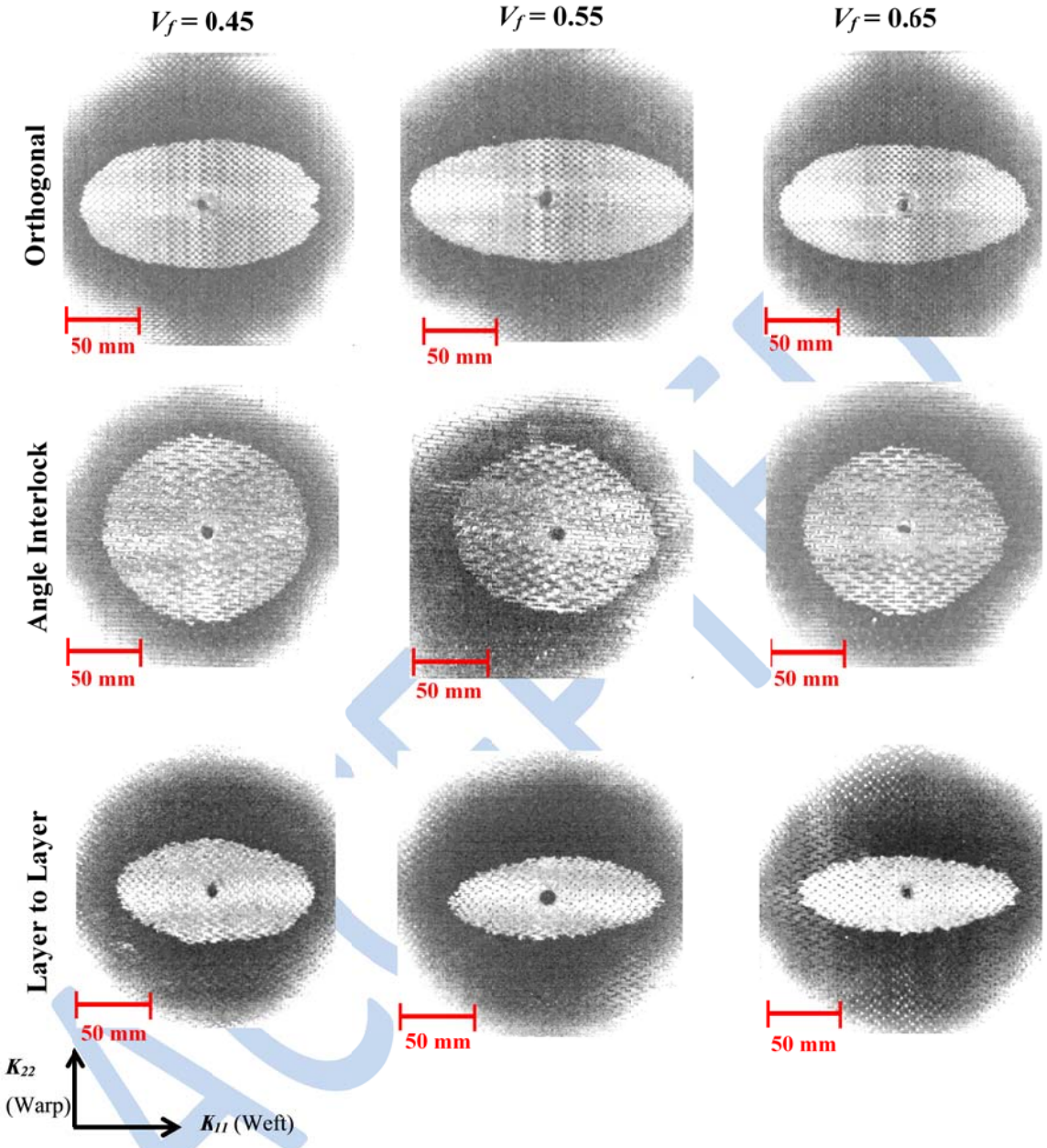

Figure 6. Flow front progression during in-plane permeability tests at V_f = 0.45, 0.55 and 0.65 of (a) orthogonal, (b) angle interlock, and (c) layer to layer fabrics.

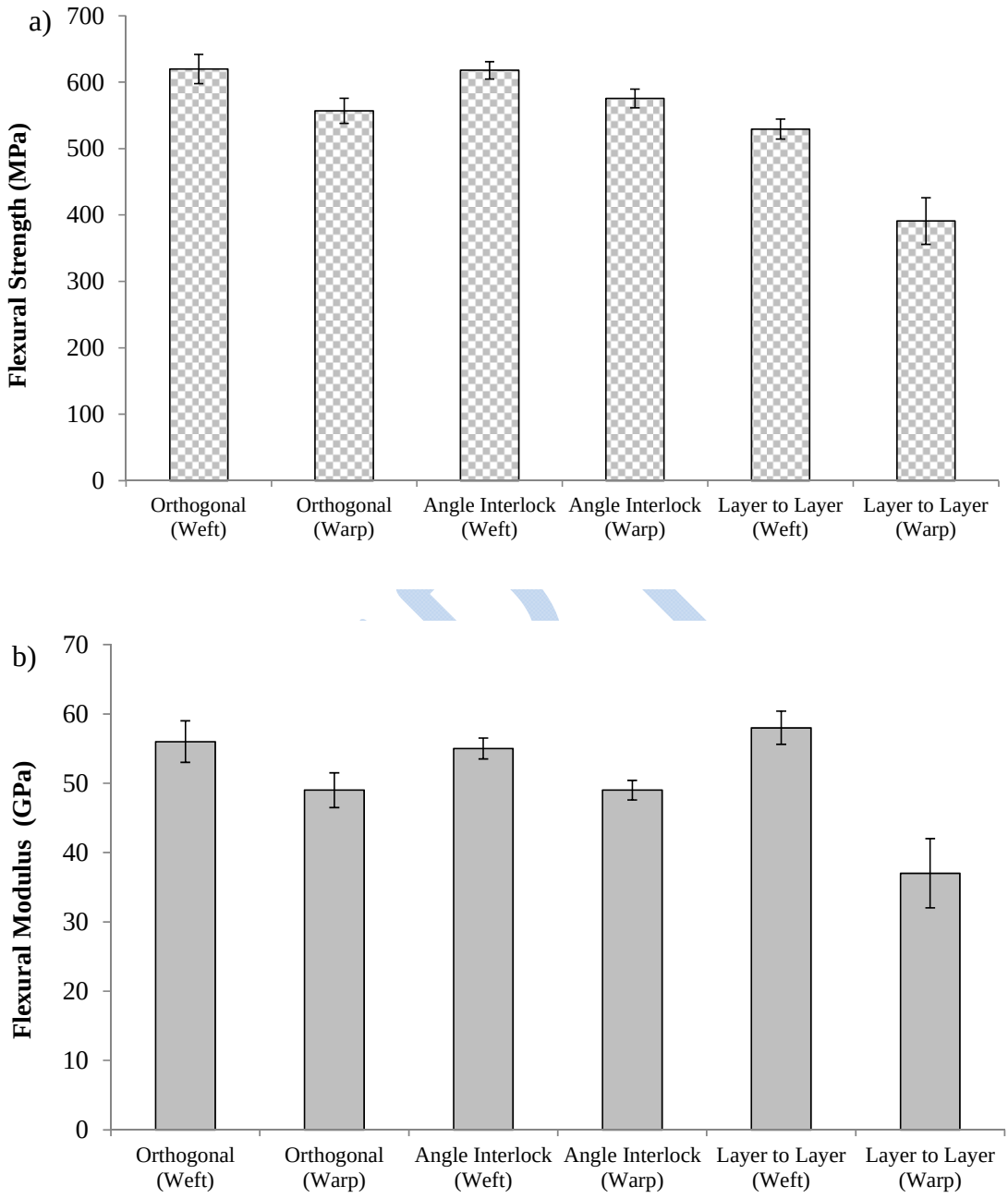

Figure 7. Summary of the flexural properties of the 3D fabric composites (a) flexural strength and (b) flexural modulus.

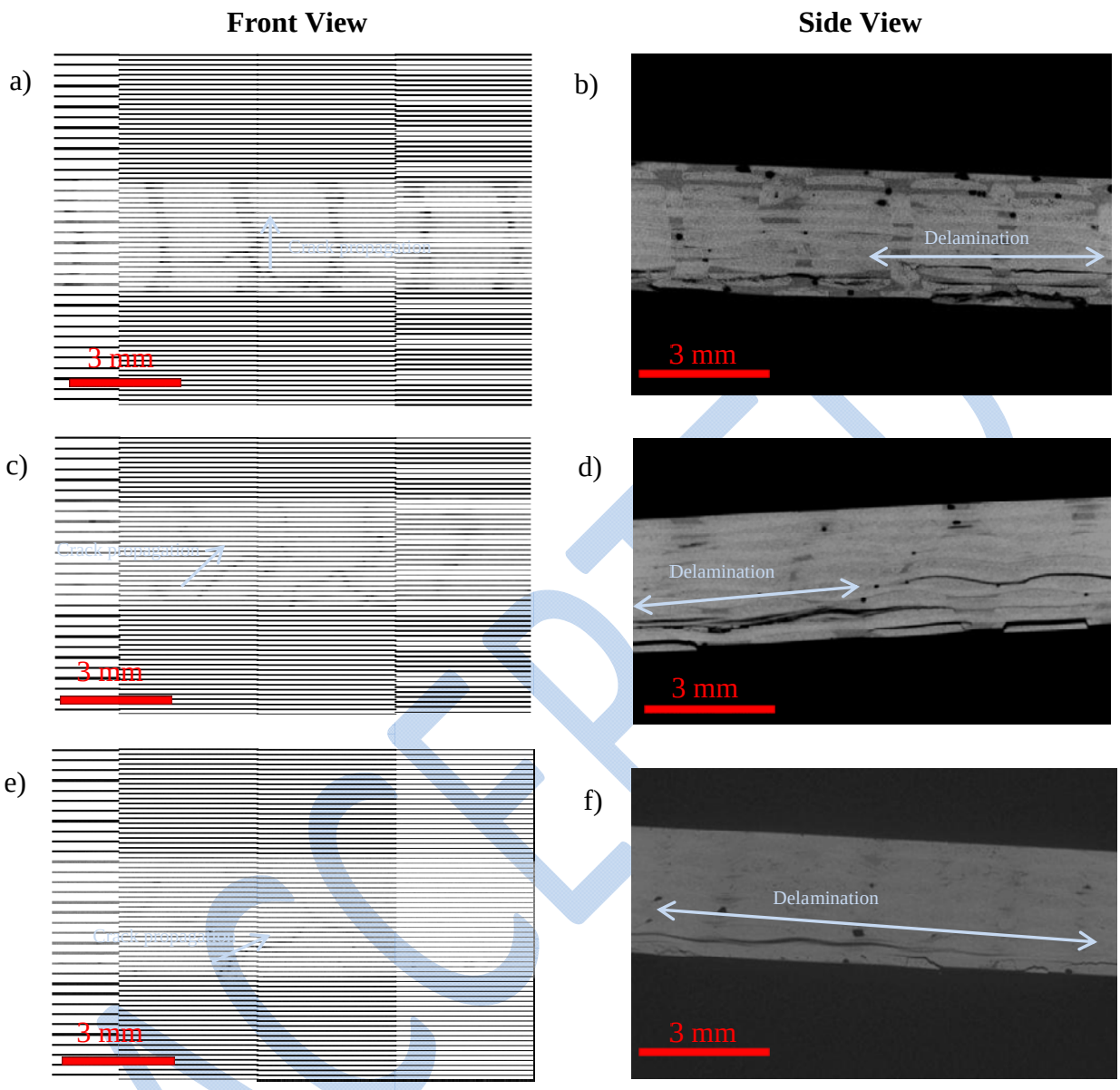

Figure 8. XCT scans of front and side of samples tested after flexural tests (a,b) Orthogonal, (c, d) Angle Interlock, (e,f) Layer to layer.

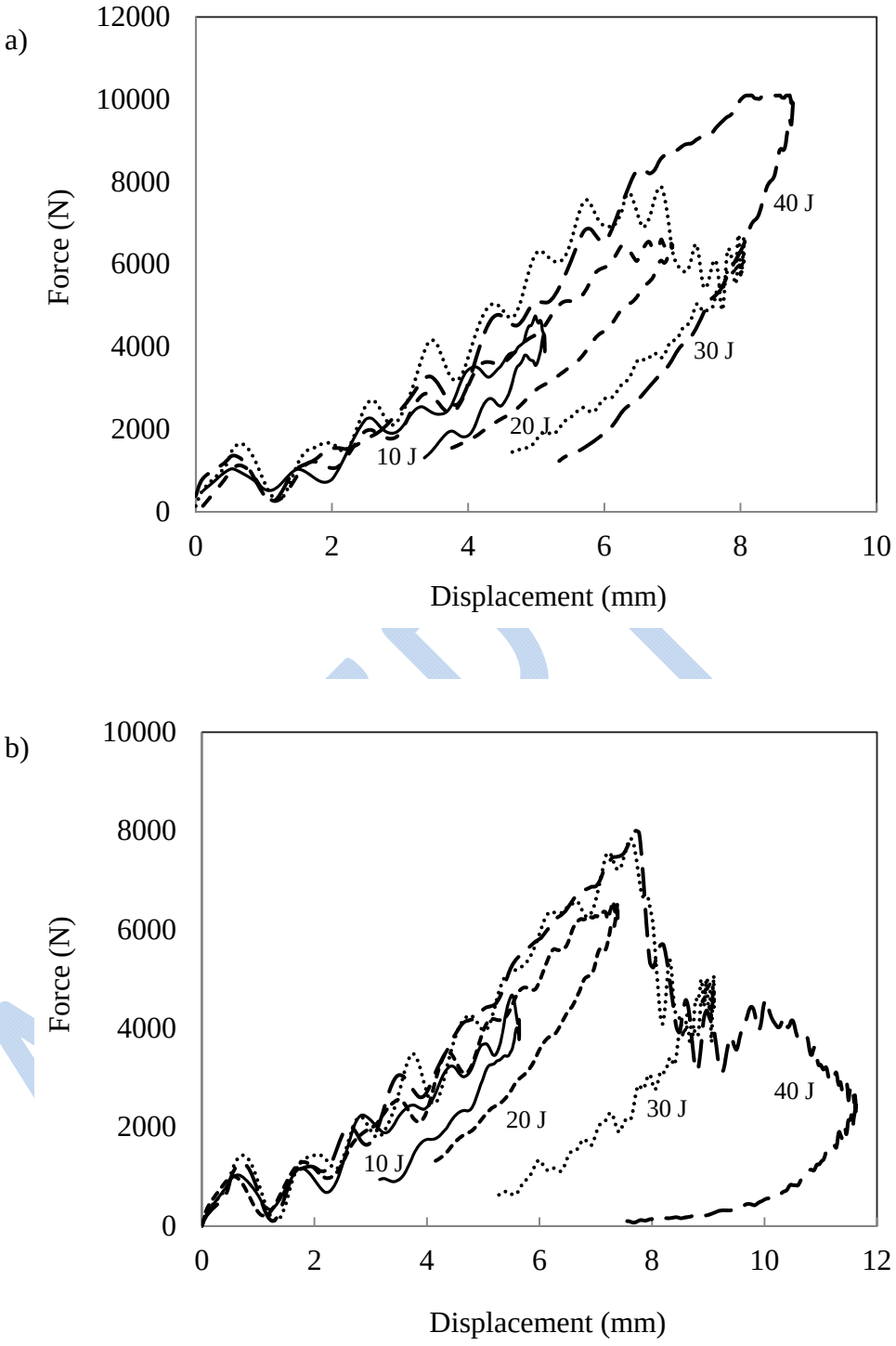

Figure 9. Load-displacement traces following low velocity impact tests on of 3D fabrics (a) Orthogonal, (b) Angle interlock. The incident impact energies are marked on the appropriate traces.

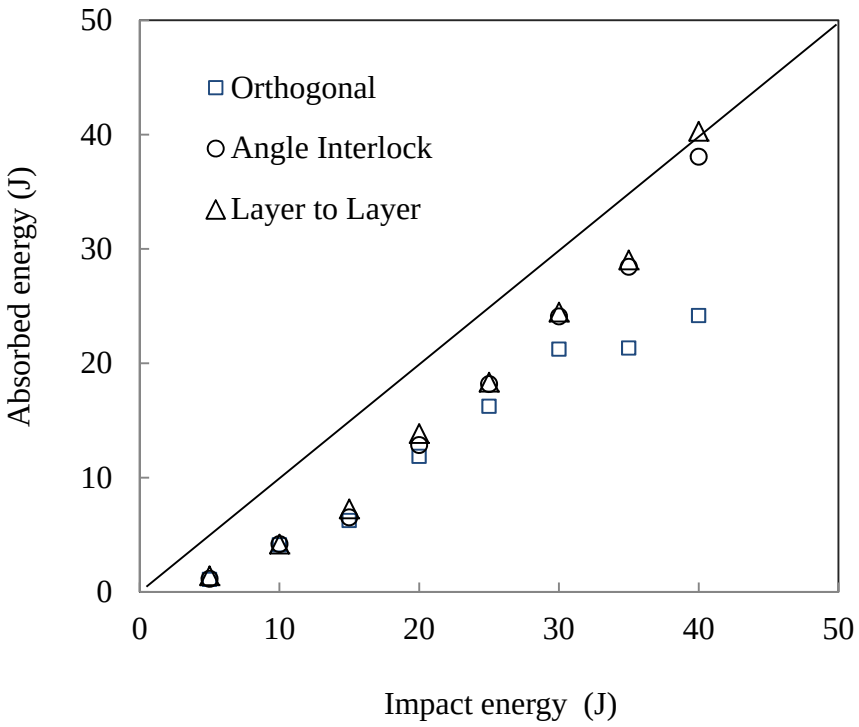

Figure 10. The variation of absorbed energy with impact energy for the 3D fabrics composites (a) Orthogonal, (b) Angle interlock, (c) Layer to layer composites.

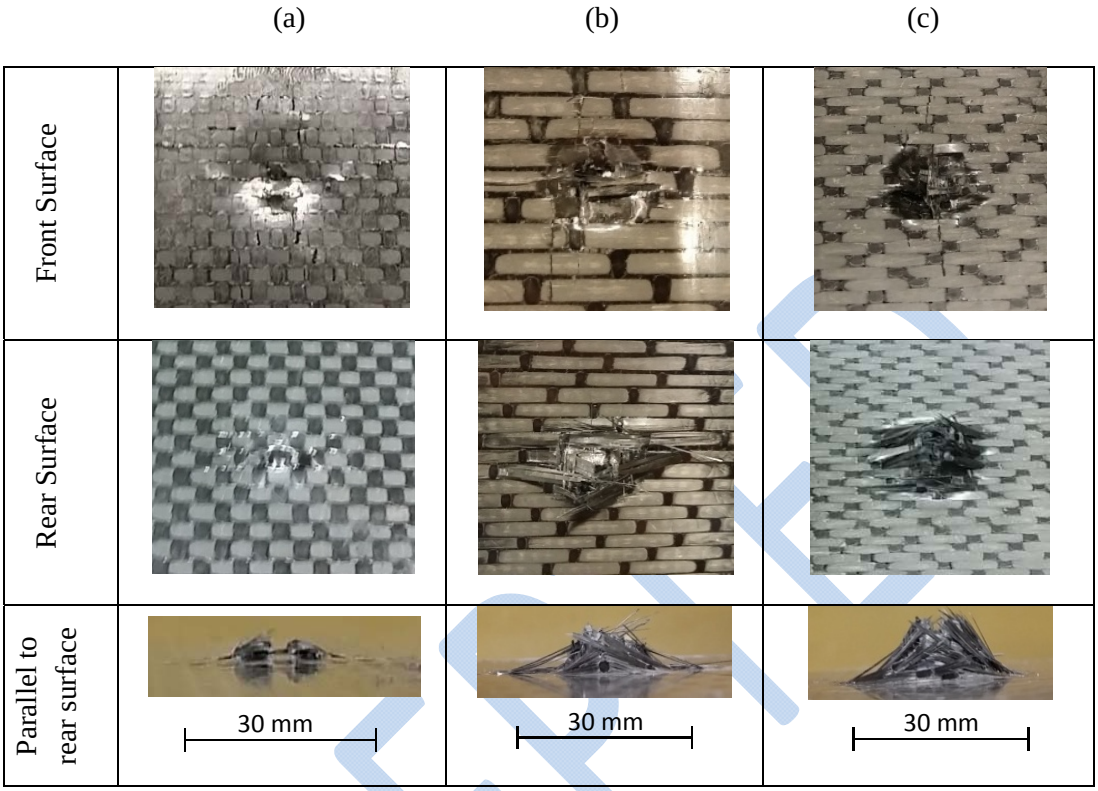

Figure 11. Comparison of the front and rear surfaces of the 3D fabrics composites following a 40 Joule impact (a) Orthogonal, (b) Angle interlock, (c) Layer to layer.

a)

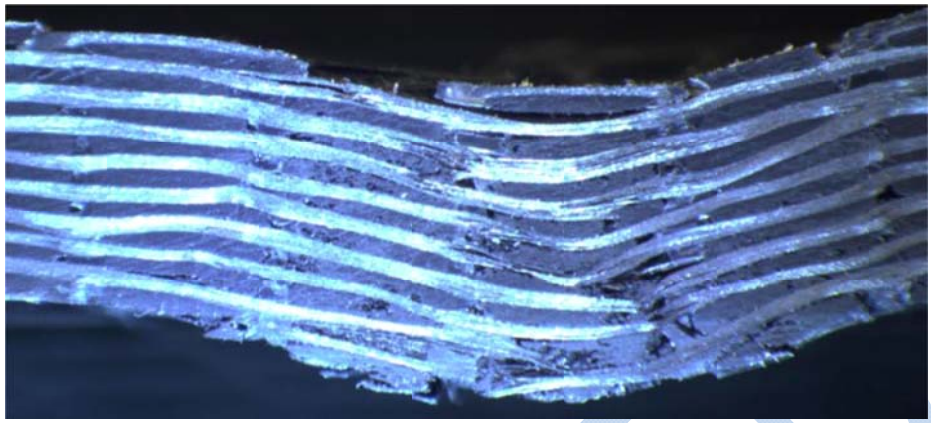

b)

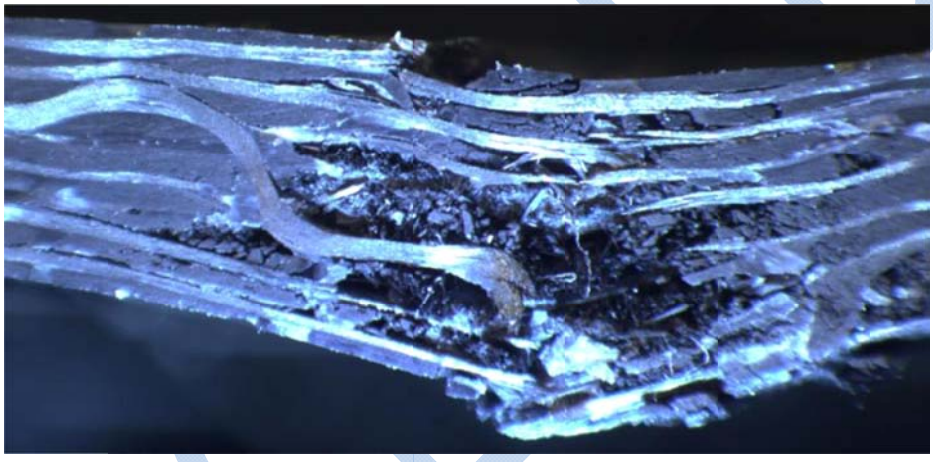

c)

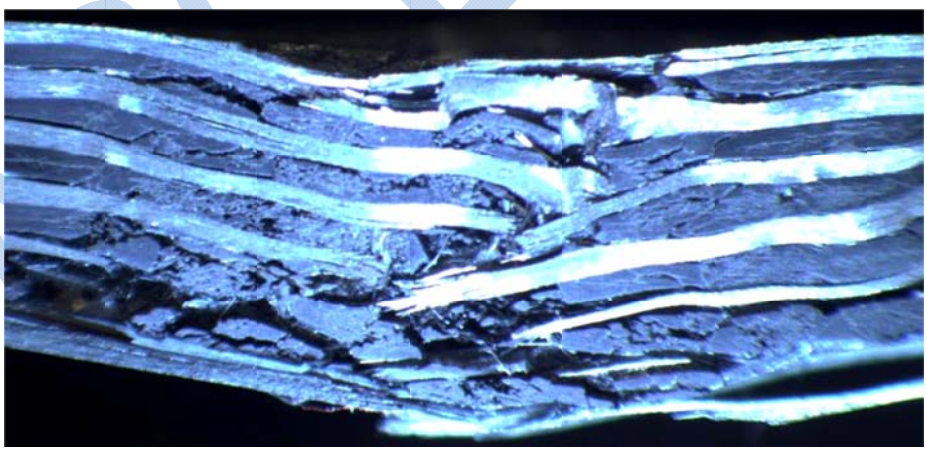

Figure 12. Cross-section of 3D composites (a) Orthogonal, (b) Angle interlock, (c) Layer to layer. Impact energy = 25 Joules. (Magnification X12).

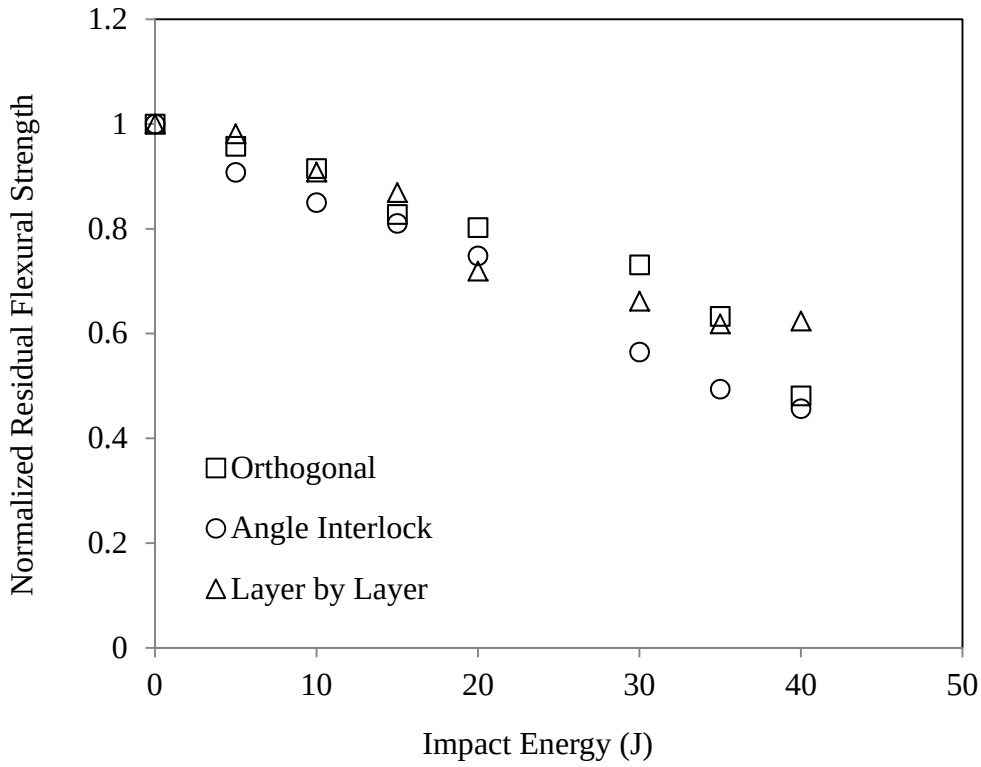

Figure 13. The variation of the composite plates with impact energy.